applied sciences

MDPI

Article

Extension of the Discrete Electron Transport Capabilities of the Geant4-DNA Toolkit to MeV Energies

Ioanna Kyriakou [1,*], Hoang N. Tran [2], Laurent Desorgher [3], Vladimir Ivantchenko [4], Susanna Guatelli [5], Giovanni Santin [6], Petteri Nieminen [6], Sebastien Incerti [2] and Dimitris Emfietzoglou [1]

[1] Medical Physics Laboratory, Department of Medicine, University of Ioannina, 45110 Ioannina, Greece; demfietz@uoi.gr
[2] University of Bordeaux, CNRS, LP2I Bordeaux, UMR 5797, F-33170 Gradignan, France; tran@cenbg.in2p3.fr (H.N.T.); incerti@cenbg.in2p3.fr (S.I.)
[3] Institute of Radiation Physics (IRA), Lausanne University Hospital, University of Lausanne, CH-1007 Lausanne, Switzerland; laurent.desorgher@chuv.ch
[4] CERN, CH-1211 Genève, Switzerland; vladimir.ivantchenko@cern.ch
[5] Centre for Medical Radiation Physics, University of Wollongong, Wollongong, NSW 2522, Australia; susanna@uow.edu.au
[6] ESA/ESTEC Space Environments and Effects Section, ESTEC, Keplerlaan 1, 2200 AG Noordwijk, The Netherlands; giovanni.santin@esa.int (G.S.); petteri.nieminen@esa.int (P.N.)
* Correspondence: ikyriak@uoi.gr

Abstract: The discrete physics models available in the Geant4-DNA Monte Carlo toolkit are a subject of continuous evolution and improvement in order to meet the needs of state-of-the-art radiobiological research for medical and space applications. The current capabilities of Geant4-DNA for event-by-event electron transport extend up to 1 MeV. In this work, Geant4-DNA's most accurate electron inelastic model for sub-keV energies is improved and extended up to 10 MeV via the Relativistic Plane Wave Born Approximation and other theoretical considerations. Benchmark simulations of the electronic stopping power and range of electrons in liquid water using the new model show almost excellent agreement (at the few % level) with the recommendations of the International Commission on Radiation Units and Measurements (ICRU) up to 10 MeV, offering notable improvement (by a factor of ~2) over the default Geant4-DNA inelastic model and an order-of-magnitude higher electron limit. The present development will allow Geant4-DNA users to perform electron track-structure simulations up to 10 MeV, thus, covering a wider range of radiotherapeutic applications (including FLASH-RT) as well as space applications involving MeV electrons which are not currently reachable.

Keywords: Monte Carlo; Geant4-DNA; truck structure; stopping power; cross sections

Academic Editor: Vladislav Toronov

Received: 16 October 2024
Revised: 11 January 2025
Accepted: 16 January 2025
Published: 24 January 2025

Citation: Kyriakou, I.; Tran, H.N.; Desorgher, L.; Ivantchenko, V.; Guatelli, S.; Santin, G.; Nieminen, P.; Incerti, S.; Emfietzoglou, D. Extension of the Discrete Electron Transport Capabilities of the Geant4-DNA Toolkit to MeV Energies. *Appl. Sci.* **2025**, *15*, 1183. https://doi.org/10.3390/app15031183

1. Introduction

Monte Carlo (MC) track-structure (TS) simulations are an established tool for quantitative analysis of radiation effects at the cellular and DNA levels [1]. The strength of MCTS simulations rests on their ability to model (charged) particle interactions in a discrete manner according to the corresponding single-scattering cross sections. Thus, the MCTS approach is capable of revealing, at the highest level of detail, the spatial pattern of energy deposition in the medium. Another distinct advantage of MCTS simulations, that follows from their molecular-scale resolution, is the potential to go beyond the physical stage and simulate the subsequent radiolysis of water, which underlines the so-called indirect radiation action in cells, as well as the initial DNA damage along with its degree of complexity [2–5]. Currently, there exist more than thirty MCTS codes (reviewed

in [6–8]) which have been developed specifically for radiobiological applications, including micro- and nano-dosimetry. These codes differ mainly on the interaction cross sections used for simulating the transport of charged particles (mainly electrons) in a liquid water medium, although they may further differ regarding the details of the modeling of the physico-chemical reactions and biological damage, if available [9–13]. However, except for the Geant4-DNA toolkit [8,14–17], all currently available MCTS codes are not publicly available, they are the propriety of the investigator (or research group), which limits their usage by the broader community of researchers in the field. Therefore, as far as we know, there is no systematic intercomparison of MCTS codes (apart from [10] which is limited to only two codes). Because the amount of input data and computing time increases rapidly with particle energy, MCTS simulations are not currently used in clinical practice where energies are usually in the MeV (or MeV/amu) range. In clinical applications, MC simulations by the condensed-history approach are the preferred choice because they are much faster than MCTS simulations and are also easily extended to different transport media. However, conventional MC simulations using the condensed-history technique are not suitable for nanometer (or molecular) scale resolution, due to the inherent limitations of the condensed-history technique [8,18].

Although MCTS simulations are traditionally applied to the transport of low-energy particles, e.g., electrons with energies below 10–100 keV, there is an increasing interest in extending their application to higher energies, in order to cover the full radiotherapeutic domain, including some emerging modalities like FLASH [19–23]. This interest mainly comes from the need to link the physical stage of radiation action (e.g., via micro- or nano-dosimetry) to the radiobiological effects and provide the ground for developing biophysical or mechanistically inspired dose–response models [24,25]. Among other things, such models are potentially useful for the development of robust radiobiological-based optimization of treatment planning systems [26,27].

Apart from conventional electron beam radiotherapy (EBRT), which uses electron beams in the 6–18 MV energy range [28], energetic electrons (~MeV) are also of interest for risk estimates from space radiation exposure of crewed missions [29–34]. These include studies of the Van Allen outer belt, which consists of electrons up to about 10 MeV, as well as the energetic delta rays produced by the GeV/amu ions of the galactic cosmic ray (GCR) spectrum [35–37]. In addition, emerging treatment technologies, like FLASH radiotherapy, which use high energy electrons as a primary beam, require MCTS simulations up to several MeV, as a means to explore the radiobiological FLASH effect which relates to the spatial distribution of radiolytic species [38–40].

Owing to the special role of electrons (both as primary and secondary particles) in MCTS simulations, the Geant4-DNA toolkit [8,14–17], includes a variety of different physics models to describe each type of interaction (i.e., ionization, electronic excitation, and elastic scattering). Furthermore, there are some ready-to-use sets of physics models for Geant4-DNA users, known as “constructors”, that gather the most significant physical processes [8,17]. Although important efforts are currently invested to describe electron interactions in DNA-like materials using measured or calculated cross sections for individual DNA bases (in the gas phase) [41,42], liquid water remains the most generic transport media in radiobiological applications, since cells are mostly composed of water (70–80% by weight), which is also the source of reactive free-radicals. The different “constructors” (and physics models) for liquid water medium currently available in Geant4-DNA have been described in detail in previous works [43–45].

Historically, an important challenge to the development of MCTS codes is the calculation of low-energy inelastic cross sections for all the ionization shells and electronic excitation levels of the irradiated medium down to threshold energies (~10 eV). Nowadays,

the most established MCTS codes for liquid water calculate inelastic cross sections via a semi-empirical model of the dielectric response function of the medium [1,9,11,46–49]. The attractive feature of this approach is that condensed-phase effects, which are crucial for modeling radiation interactions in biological matter at the nanoscale, are in-built into the methodology.

Currently, the most accurate low-energy electron inelastic model in Geant4-DNA is implemented into the DNA-Opt4 constructor [43,44]. However, its upper energy limit of 10 keV, prohibits using it in many practical (e.g., clinical) applications. So, in order to cover medium–high energy applications, Geant4-DNA users need to combine DNA-Opt4 (<10 keV) with the default constructor DNA-Opt2 (>10 keV) [17]. Therefore, the extension of the inelastic model of DNA-Opt4 to higher electron energies (its elastic model is already applicable to relativistic energies) has become a "physics-activity" priority for the Geant4-DNA collaboration. To that end, a preliminary relativistic extension of DNA-Opt4 was recently presented (referred to as DNA-Opt4Rel in [50]), focusing mostly on refinements of the dielectric response function and the presentation of the needed relativistic modifications to reach Geant4-DNA's current upper electron limit of 1 MeV.

The aim of this work is to document a complete relativistic version of the inelastic model of DNA-Opt4 (hereafter termed DNA-Opt4X) which improves and extends Geant4-DNA capabilities up to 10 MeV. The full set of ionization and excitation cross sections implemented into this new constructor (DNA-Opt4X) are presented, and benchmark simulations of the electronic stopping power and range of electrons in liquid water are performed and assessed against the available ICRU data. An intercomparison between the new (DNA-Opt4X) and existing inelastic models (DNA-Opt2, DNA-Opt6) of Geant4-DNA is also provided.

Unless otherwise stated, energy, momentum, and mass are expressed in units of eV, eV/c, and eV/c^2, respectively, where 1 eV = 1.602 $\times$ 10^{-19} joule and c^2 = 931.46 MeV per atomic mass unit (amu).

2. Materials and Methods

2.1. Basic Features of the Present Model

In both DNA-Opt2 (default constructor) [15] and DNA-Opt4 (recommended low-energy constructor) [43,44], the inelastic model used to calculate the excitation and ionization cross sections is based on a semi-empirical dielectric response function determined by an optical-data model [8]. This approach is considered the state-of-the-art for practical calculations of inelastic electron-scattering in condensed medium (e.g., liquids, solids) [1,9,11,46–49], as it is based on the well-established theoretical framework of the first Born approximation while offering a reasonable balance between computational simplicity and robustness. Although ab initio approaches offer far more detail and are theoretically rigorous [51,52], they are still not as attractive as the semi-empirical optical-data models, at least for those materials (like liquid water) where experimental optical data are available, due to their theoretical complexity and higher computational cost. Optical-data models commonly employ either a Drude-type or a Lindhard-type or a Mermin-type representation of the dielectric function [1,46–49]. The Drude-type representation, which is mathematically (and computationally) simpler, is used in both DNA-Opt2 and DNA-Opt4, as well as by other popular MCTS codes for liquid water, like NOREC [53], PARTRAC [54], and KURBUC [55].

The theoretical framework adopted in the present work for the calculation of electron inelastic cross sections is the Relativistic Plane Wave Born Approximation (RPWBA) where the probability of ionization and excitation of the medium is essentially described by the energy loss function (ELF) which is defined by the imaginary part of the reciprocal

dielectric function (see below). The present inelastic model, hereafter denoted as "DNA-Opt4X", includes all the latest modifications to the ELF (presented in [43,44,50]) that reduced the sum-rule errors to less than 1.5% (from 6.5% in DNA-Opt2). In addition, both the low- and high-energy corrections are implemented as described in [50]. However, to efficiently extend the model above 1 MeV, additional corrections and modifications have been implemented as will be described in the next sections. Since the various corrections involve additional cross section calculations (which are often far more time-consuming per data point than the uncorrected calculations), we restrict the application of each correction to specific energy regimes where a sizeable impact is expected (see Figure 1). The optimum transition energy (from one regime to the next) may depend on the application. As a first approximation, we here adopt a more general approach (also used in [50]) where the transition energy is based on the impact of the correction to a fundamental and well-understood radiation dosimetry quantity, namely, the electronic stopping power. Therefore, corrections are applied only within the energy range in which their individual effect on the electronic stopping power is larger than 1%. Based on this criterion, and in order to make the model implementation more transparent to future modifications, we distinguish between four energy regimes as depicted in Figure 1.

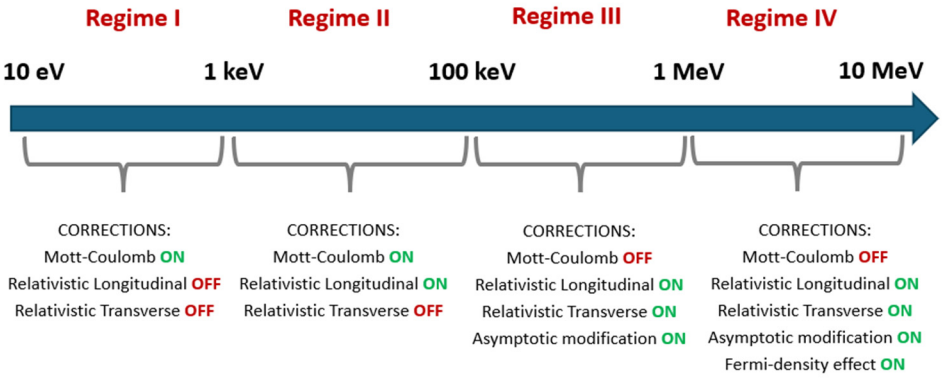

Figure 1. Schematic of the different correction terms implemented into the present inelastic model (DNA-Opt4X). To reduce the computational burden, corrections are turned "ON/OFF" only within the energy range (regime) in which they have an effect larger/smaller than 1% to the electronic stopping power (SP).

In the existing dielectric models of Geant4-DNA, the inelastic cross sections are calculated off-line and implemented into the code via look-up tables, so the complexity of the inelastic physics model does not have any impact on the simulation running times (apart from the rather small influence of the different energy binning between different models). Thus, the implementation (or not) of the various corrections (see Figure 1) does not (practically) influence simulation running times. However, simulations by DNA-Opt4X are faster (depending on the specific application) than the current default constructor (DNA-Opt2) due to the different elastic models used. This effect has also been observed with the existing DNA-Opt4, but it is expected to be even more pronounced with DNA-Opt4X due to the two orders of magnitude higher energy range of application.

2.2. Implementation of the Plane Wave Born Approximation (PWBA)

The analytic representation of the dielectric function $\varepsilon(E,q) = \varepsilon_1(E,q) + i\varepsilon_2(E,q)$, with E being the energy transfer and q the momentum transfer, is based on the same methodology used in DNA-Opt2 and DNA-Opt4. Specifically, a sum of Drude-type functions is used to parameterize the experimental optical data ($q = 0$) for $\varepsilon_2(E, q = 0)$ and $\varepsilon_1(E, q = 0)$ which are then extended to non-zero q (for arbitrary E) by analytic dispersion relations implemented into the Drude coefficients, which ensure the proper asymptotic limits at both

small- and large-q. The contribution of individual ionizations and excitation transitions to $\varepsilon_2(E,q)$ is obtained by an in-house deconvolution algorithm [43,44] for $\varepsilon_2(E,q)$, which introduces threshold energies (e.g., shell binding energies), conserves the sum-rules, and allows $\varepsilon_1(E,q)$ to be obtained analytically by the Kramers–Kronig relation. Then, the complete ELF along with its partitioning to ionizations and excitations reads as follows:

$$\mathrm{ELF} = \mathrm{Im}\left[-\frac{1}{\varepsilon(E,q)}\right] = \sum_{j}^{ioniz} \underbrace{\frac{\varepsilon_2^{(j)}(E,q)}{\varepsilon_1^2(E,q)+\varepsilon_2^2(E,q)}}_{\mathrm{ELF}_{ioniz}} + \sum_{k}^{excit} \underbrace{\frac{\varepsilon_2^{(k)}(E,q)}{\varepsilon_1^2(E,q)+\varepsilon_2^2(E,q)}}_{\mathrm{ELF}_{excit}}, \tag{1}$$

where j, k correspond to the ionization and excitation transitions, respectively, which include four ionization shells (j = 1, 2, … 4) and five discrete excitation levels (k = 1, 2, …, 5) as described elsewhere [43,44,50]. These outer (or valence) inelastic channels are expected to exhibit condensed-phase properties (e.g., long-range screening) and, therefore, most appropriately treated within the present dielectric-based ELF model of Equation (1). Within the PWBA all relevant physical quantities that are needed as input to MCTS simulations can be calculated from the ELF of Equation (1) by suitable integrations over the E and q variables. The partitioning of ELF described in Equation (1) is particularly important to MCTS simulations because it allows the calculation of inelastic cross sections (both differential and integral) for the individual ionization shells and excitation levels. For example, the inelastic energy-transfer differential cross section (DCS), which is the most fundamental quantity in MCTS codes since it determines the single-collision energy-loss spectrum of the incident charged particle, is obtained by an integration of the ELF of Equation (1) over q:

$$\begin{aligned}\frac{d\sigma_{PWBA}(E;T)}{dE} &= \sum_{j}^{ioniz} \frac{d\sigma_{PWBA}^{(j)}(E;T)}{dE} + \sum_{k}^{excit} \frac{d\sigma_{PWBA}^{(k)}(E;T)}{dE} = \\ &= \frac{1}{\pi\alpha_0 NT}\left\{ \sum_{j}^{ioniz} \int_{q_{min}}^{q_{max}} \mathrm{ELF}_{ioniz}^{(j)}(E,q)\frac{dq}{q} \right. \\ &\left. + \sum_{k}^{excit} \int_{q_{min}}^{q_{max}} \mathrm{ELF}_{excit}^{(k)}(E,q)\frac{dq}{q} \right\},\end{aligned} \tag{2}$$

where $\alpha_0 = 5.29 \times 10^{-11}$ m is the Bohr radius, $N = 33.4 \times 10^{27}$ m^{-3} is the density of water molecules in liquid water, and the limits of the momentum transfer (q) in the non-relativistic case are

$$q_{min/max} = \sqrt{2m}\left(\sqrt{T} \pm \sqrt{T-E}\right). \tag{3}$$

Subsequent integration of the DCS of Equation (2) over E yields the total (integral) cross section (TCS) for inelastic collisions:

$$\begin{aligned}\sigma_{PWBA}(T) &= \sum_{j}^{ioniz} \sigma_{PWBA}^{(j)}(T) + \sum_{k}^{excit} \sigma_{PWBA}^{(k)}(T) \\ &= \frac{1}{\pi\alpha_0 NT}\left\{ \sum_{j}^{ioniz} \int_{E_{min,j}}^{E_{max,j}} \int_{q_{min}}^{q_{max}} \mathrm{ELF}_{ioniz}^{(j)}(E,q)\frac{dq}{q} \right. \\ &\left. + \sum_{k}^{excit} \int_{E_{min,k}}^{E_{max,k}} \int_{q_{min}}^{q_{max}} \mathrm{ELF}_{excit}^{(k)}(E,q)\frac{dq}{q} \right\},\end{aligned} \tag{4}$$

where the integration limits of the energy transfer are $E_{\min(j,k)} = B_{(j,k)}$, $E_{\max,j} = \left(T + B_j\right)/2$, and $E_{\max,k} = T$ with B_j and B_k being the binding energy of the j-th ionization shell and the transition energy of the k-th excitation level, respectively, of the medium. Note that, as written in Equations (2) and (3), σ corresponds to the so-called macroscopic cross section or inverse mean free path with units 1/length.

Similar to the existing dielectric-based inelastic models (i.e., DNA-Opt2 and DNA-Opt4), the application of the dielectric function approach to DNA-Opt4X is restricted to the outer-shell (or valence) electrons of liquid water (i.e., to ionization shells j = 1–4 and excitation levels k = 1–5) where the influence of long-range polarization due to the condensed phase is most pronounced. Inelastic cross sections for the ionization of the innermost shell of H_2O (i.e., of ionization shell j = 5) are calculated by a relativistic extension of the binary-encounter-approximation-with-exchange (BEAX) model [56,57].

2.3. Low-Energy Corrections

The PWBA is known to be a good approximation for electrons with incident energies much larger than the binding energies of target electrons. For liquid water medium, the application of the PWBA to the outer-shell target electrons (with binding energies between ~10–30 eV) is well justified for electrons above ~1 keV. Since the present model (DNA-Opt4X) is meant to be applicable down to 10 eV, "low-energy" corrections to the PWBA must be applied at sub-keV energies. The Mott–Coulomb low-energy corrections included in the default inelastic model (DNA-Opt2) [15] have been already re-assessed and improved in the context of DNA-Opt4 [43,44]. These improved low-energy corrections are also passed into the present inelastic model (DNA-Opt4X). However, the magnitude of these Mott–Coulomb corrections for particular transitions may be different among the existing DNA-Opt4 and the present DNA-Opt4X. To illustrate this point, we summarize the final expressions. For ionizations, the Mott–Coulomb corrected DCS and TCS read as follows:

$$\frac{d\sigma^{(j)}_{Mott-Co}(E;T)}{dE} = \frac{d\sigma^{(j)}_{PWBA}\left(E;T+B_j+U_j\right)}{dE} + \frac{d\sigma^{(j)}_{PWBA}\left(T+2B_j+U_j-E;T+B_j+U_j\right)}{dE} - \sqrt{\frac{d\sigma^{(j)}_{PWBA}\left(E;T+B_j+U_j\right)}{dE} \times \frac{d\sigma^{(j)}_{PWBA}\left(T+2B_j+U_j-E;T+B_j+U_j\right)}{dE}}, \quad (5)$$

and

$$\sigma^{(ioniz)}_{Mott-Co}(T) = \sum_{j}^{ioniz} \int_{E_{min,j}}^{E_{max,j}} \frac{d\sigma^{(j)}_{Mott-Co}(E;T)}{dE} dE, \quad (6)$$

with U_j being the electron kinetic energy in the j-th ionization shell. For excitations, only Coulomb corrections are applied:

$$\sigma^{(excit)}_{Co}(T) = \sum_{k}^{excit} \sigma^{(k)}_{PWBA}(E;T+2B_k). \quad (7)$$

Evidently, the Mott–Coulomb corrected cross sections, Equations (5)–(7), depend explicitly upon the ELF and its parameterization, which is somewhat different between DNA-Opt4 and DNA-Opt4X. Following the criterion discussed above (see Figure 1), the Mott–Coulomb corrections, Equations (5)–(7), are only applied in the energy Regimes I and II.

2.4. Relativistic Corrections

In the context of the Relativistic Plane Wave Born Approximation (RPWBA), the DCS is commonly written as the sum of a longitudinal and transverse term:

$$\frac{d\sigma_{RPWBA}(E;T)}{dE} = \frac{d\sigma_{\text{Longitudinal}}(E;T)}{dE} + \frac{d\sigma_{\text{Transverse}}(E;T)}{dE}. \quad (8)$$

An in-depth discussion of RPWBA calculations for condensed matter systems is provided by Fernández-Varea et al. [57]. Similar to the non-relativistic limit, the longitudinal

term in Equation (8) is determined by an integration of the ELF over q. However, due to relativistic kinematics, the final expression differs from Equation (2) and reads as follows:

$$\begin{aligned}\frac{d\sigma_{\text{Longitudinal}}(E;T)}{dE} &= \sum_{j,k}^{ioniz,excit} \frac{d\sigma^{(j,k)}_{\text{Longitudinal}}(E;T)}{dE} \\ &= \frac{1}{\pi\alpha_0 N mc^2\beta^2}\left\{\sum_{j,k}^{ioniz,excit} \int_{q_{min,rel}}^{q_{max,rel}} \text{ELF}^{(j,k)}(E,q)\frac{dq}{q}\right\} \\ &= \frac{1}{\pi\alpha_0 N mc^2\beta^2}\int_{q_{min,rel}}^{q_{max,rel}} \left(\frac{c^2 q}{\sqrt{c^2q+(mc^2)^2}}\right)\frac{1+\frac{Q(q)}{mc^2}}{1+\frac{Q(q)}{2mc^2}} ELF(E,q)\frac{dq}{Q(q)},\end{aligned} \tag{9}$$

where $Q = \sqrt{c^2q^2 - (mc^2)^2} - mc^2$ is the relativistic free-recoil energy (with c the speed of light) and $\beta^2 = \frac{v^2}{c^2} = 1 - \frac{1}{\sqrt{\left(\frac{T}{mc^2}+1\right)}}$. The limits of the q-integration at relativistic energies are as follows:

$$q_{max,rel/min,rel} = \frac{1}{c}\left[\sqrt{T(T+2mc^2)} \pm \sqrt{(T-E)(T-E+2mc^2)}\right]. \tag{10}$$

Following the criterion discussed above (see Figure 1), the longitudinal term, Equation (9), replaces Equation (2) in the energy Regimes II, III, and IV. Note that in Regime II the Mott–Coulomb corrections are applied to the Longitudinal term of the RPWBA, Equation (9), which should replace the "PWBA" term in Equations (5)–(7).

For the transverse term in Equation (8), we follow common practice and use Fano's small angle scattering approximation [58]. This approximation makes the transverse term depend only on the optical limit of ELF as follows:

$$\begin{aligned}\frac{d\sigma_{\text{Transverse}}(E;T)}{dE} &= \sum_{j,k}^{ioniz,excit} \frac{d\sigma^{(j,k)}_{\text{Transverse}}(E;T)}{dE} \\ &= \frac{1}{\pi\alpha_0 N mc^2\beta^2}\left\{\sum_{j,k}^{ioniz,excit} \text{ELF}^{(j,k)}(E,q=0)\right\}\left[\ln\left(\frac{1}{1-\beta^2}\right) - \beta^2\right].\end{aligned} \tag{11}$$

Note that Equation (11) vanishes at the non-relativistic limit. Following the criterion discussed above (see Figure 1), the transverse term, Equation (11), is considered only in the energy Regimes III and IV.

An additional relativistic correction that sets in at condensed media and energies above the rest-mass energy of the projectile is the Fermi density effect correction [59]. It is related to the weakening of the Coulomb force experienced by distant atoms due to the enhancement of screening that arises from length contraction. This correction affects only distant ($q = 0$) transverse interactions. Note that the density effect correction is not included in the recent relativistic version of DNA-Opt4 (called DNA-Opt4Rel) [50]. We have implemented the Fermi density effect correction to the DCS following the formalism of Fernández-Varea et al. [57], which yields the following expression:

$$\frac{d\sigma_{\text{Transverse},\delta}(E;T)}{dE} = \delta_F \frac{d\sigma_{\text{Transverse}}(E;T)}{dE}, \tag{12}$$

where δ_F is the density effect parameter. According to Fano [60,61], δ_F is linked to parameters related to the optical oscillator strength or, equivalent, to the ELF($E, q = 0$). In

the present work, we have used the analytical approach by Steinheimer et al. [61] with parameters related to liquid water medium [58].

$$\delta(X) = \begin{cases} 4.6052X + \alpha(X_1 - X)^m + C, \; X_0 < X < X_1 \\ 4.6052X + C, \; X > X_1 \end{cases}, \quad (13)$$

where $X = log_{10}\left(\frac{\beta}{\sqrt{1-\beta^2}}\right)$. The other parameters of Equation (13) are provided by the corresponding tables from [61]. For liquid water, we have used α = 0.09116; X_1 = 2.8004; m = 3.4773; C = −3.5017; X_0 = 0.24. Following the criterion discussed above (see Figure 1), the density effect correction, Equations (12) and (13) is added only in the energy Regimes IV.

Finally, it is well known that the Drude-based ELF, although very convenient at low-intermediate energies, exhibits undesirable asymptotic properties at high energies. Specifically, at sufficiently large energy transfers (i.e., above inner-shell thresholds), long-range screening effects vanish, so the following relation holds: $\mathrm{Im}\left[-\frac{1}{\varepsilon(E)}\right] \approx \mathrm{Im}[\varepsilon(E)] \equiv \varepsilon_2(E)$. However, $\varepsilon_2(E)$ is proportional to $(1/E)df(E)/dE$, where $df(E)/dE$ is the optical oscillator strength distribution which, for hydrogen-like systems, reduces asymptotically according to $df(E)/dE \sim E^{-3.5}$. Therefore, for such systems, $\mathrm{Im}\left[-\frac{1}{\varepsilon(E)}\right]$ and $\varepsilon_2(E)$ should decrease asymptotically as $E^{-4.5}$ [46]. However, the Drude-based ELF of Equation (1) used in the present model decreases by E^{-3}, as can be trivially deduced from the analytic properties of the Drude function [46]. Although water is not hydrogen-like, it is expected according to the above reasoning that the Drude-type ELF may still overestimate the "true" ELF of liquid water at sufficiently high E. For example, the somewhat higher I-value commonly obtained by this methodology may be traced to the above overestimation. In an effort to minimize this effect, we have applied an ad hoc asymptotic correction to the ELF at energy transfers above 50 keV (i.e., incident electron energies above ~100 keV) which yields a steeper reduction to the ELF and improves agreement with the SP data of the ICRU Report 90 [59] (see below). Following the criterion discussed above (see Figure 1), the asymptotic correction is added in the energy Regimes III and IV.

2.5. Stopping Power (SP) and Range (R)

Knowledge of the inelastic cross section for all ionization shells and excitation levels allows the calculation of the (electronic) SP, i.e., the mean energy loss per pathlength, from first principles, using the expression:

$$\mathrm{SP}(T) = -\frac{dT}{dx} = N\sum_{j}^{ioniz.}\int_{E_{min,j}}^{E_{max,j}} E\frac{d\sigma_{ioniz.}^{(j)}(E;T)}{dE}dE + N\sum_{k}^{excit.} E_k\sigma_{excit.}^{(k)}(T). \quad (14)$$

In the present work, depending on the electron incident energy (see Figure 1), different corrections enter into Equation (14) via the expressions for $d\sigma_{ioniz.}^{(j)}/dE$ and $\sigma_{excit.}^{(k)}$. MCTS simulations of SP are practically equivalent to Equation (14) as long as the distance traveled (dx) by the particle is sufficiently small so that $dT \ll T$. At sufficiently high particle energies (e.g., electrons above ~1 keV), a convenient approximation to Equation (14) is offered by the Bethe SP formula which is also used by ICRU [59]. Importantly, the Bethe formula allows the calculation of the (electronic) SP without explicit knowledge of the inelastic cross sections, i.e., the $d\sigma_{ioniz.}^{(j)}/dE$ and $\sigma_{excit.}^{(k)}$ (see Equation (14)). Instead, the only non-trivial quantity in the Bethe SP formula is the so-called I-value of the medium which depends upon the ELF at the limit of $q \to 0$. The latter quantity can be both measured and calculated. On the basis of such data, a reasonably accurate I-value for liquid water has been recommended by ICRU equal to 78 eV [58] and used to calculate SP values via Bethe's

formula with an uncertainty of 0.5–1% for $T > 100$ keV, 1–1.5% for $100 \geq T \geq 10$ keV, and 1.5–5% for $10 > T \geq 1$ keV. Due to the approximations used in Bethe's formula, uncertainties increase rapidly at lower energies and, therefore, ICRU does not provide SP values below 1 keV.

Another important quantity associated solely with the inelastic cross sections is the average pathlength traveled by the particle, also called the continuous slowing down approximation (CSDA) range (hereafter simply range or R_{CSDA}), which is defined by the following:

$$R_{CSDA}(T) = \int_{T_{final}}^{T_{initial}} \frac{1}{\mathrm{SP}(T)} dT. \quad (15)$$

MCTS simulations of the average pathlength of the particle, as it slows down from $T_{initial}$ to T_{final}, are practically equivalent to the CSDA range of Equation (15); although energy-loss straggling, which is automatically accounted for in the MCTS simulations, may cause Equation (15) to be somewhat larger than the MCTS values at low particle energies. Due to the limitations of the Bethe SP formula below 1 keV (discussed above), ICRU calculates the CSDA range by using Equation (15) only down to T_{final} = 1 keV and the remaining range is estimated very roughly using a linear interpolation of SP from 1 keV down to 0 eV, i.e., $R_{\mathrm{ICRU}} = R_{csda}(T_{initial} \rightarrow 1\ \mathrm{keV}) + R_{\mathrm{linear\ SP}}(T_{1\ \mathrm{keV}} \rightarrow 0)$ where $R_{\mathrm{linear\ SP}}(T_{1\ \mathrm{keV}} \rightarrow 0) = \frac{1}{2} \frac{1\ \mathrm{keV}}{SP(T=1\ \mathrm{keV})}$.

3. Results and Discussion

3.1. Inelastic Cross Sections

In Figure 2, we present calculated cross sections in the energy range from threshold up to 10 MeV for each ionization shell and excitation level using the present model (DNA-Opt4X). The cross sections exhibit the typical behavior of a rapid increase above the threshold energy of each inelastic channel and a subsequent decrease, due to the inverse proportionality to the square of the electron velocity, up to about the electron rest mass energy (~500 keV) where relativistic effects set in. At even higher energies, the so-called relativistic rise may be observed (practically above ~1 MeV). As expected, above a few tens of eV ionization cross sections become larger than the excitation cross sections. This is a direct consequence of the underlying ELF model which uses ordinary and derivative Drude functions (the latter decreasing more rapidly with energy) to model the ionization and excitation transitions, respectively.

In Figure 3, we show separately the longitudinal and transverse inelastic TCS terms for the individual ionization shells (top panel) and excitation levels (bottom panel) over the energy range from 100 keV to 10 MeV. Note that the ionization cross sections for shells $j = 1$ and $j = 2$ (for both the longitudinal and transverse terms) are indistinguishable in Figure 2 (top panel) due to the log scale. Note that the onset of the transverse contribution is set at energies above 100 keV according to the 1% criterion (see Figure 1). The same trend is observed for both the excitation and ionization cross sections as a function of electron energy; namely, the rapid decrease in the longitudinal contribution becomes more gradual for energies above the electron rest mass, whereas the transverse contribution steadily increases throughout the entire energy range. The combined effect leads to the relativistic rise observed in Figure 2.

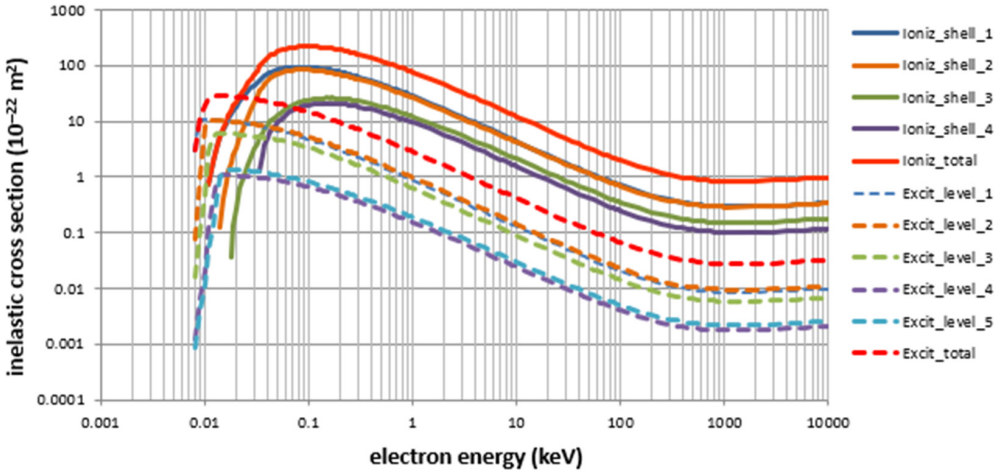

Figure 2. Electron inelastic cross sections for each (outer) ionization shell (j = 1–4) and excitation level (k = 1–5) of liquid water in the energy range from threshold (~10 eV) to 10 MeV calculated by the present model (DNA-Opt4X).

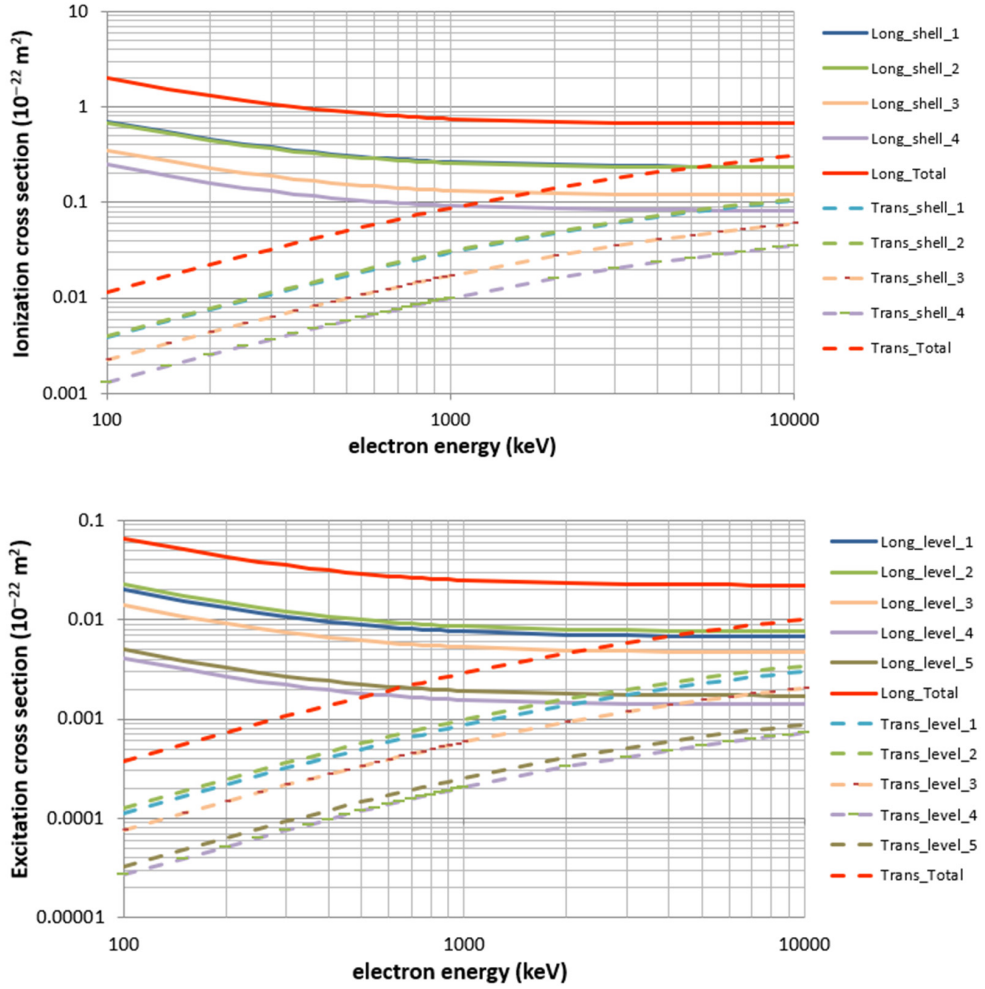

Figure 3. The longitudinal and transverse contribution to the electron inelastic cross section for each outer ionization shell (**top** panel) and excitation level (**bottom** panel) of liquid water in the energy range from 100 keV to 10 MeV calculated by the present model (DNA-Opt4X).

The relative magnitude of the longitudinal and transverse contribution to the total inelastic cross section is shown in Figure 4. It can be seen that the transverse contribution is ~1% at 100 keV, ~2% at 200 keV, ~10% at 1 MeV, and ~30% at 10 MeV. Thus, when extending MCTS simulations to electron energies beyond a few hundred keV (and especially beyond 1 MeV), the inclusion of the transverse term of the inelastic cross section is necessary so as to avoid a significant (and systematic) overestimation of the inelastic mean free path.

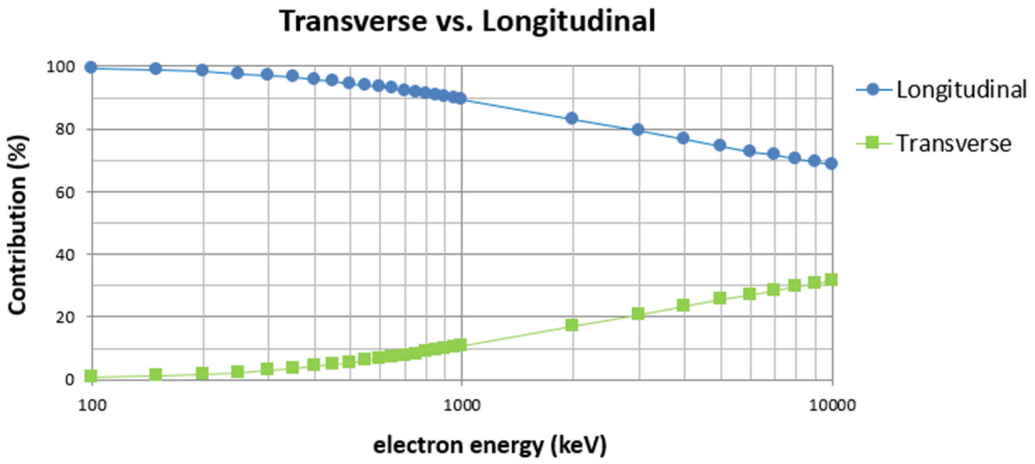

Figure 4. The contribution (in %) of the longitudinal and transverse terms to the total electron inelastic cross section of liquid water in the energy range from 100 keV to 10 MeV calculated by the present model (DNA-Opt4X).

Figure 5 shows a comparison of the total ionization (top panel) and total excitation (bottom panel) cross section between DNA-Opt2, which extends up to 1 MeV, the present model (DNA-Opt4X), which extends up to 10 MeV, and DNA-Opt6 which extends up to 256 keV. The differences at low energies are discussed elsewhere [43,44]. In brief, the differences between the two dielectric-based inelastic models (i.e., those of DNA-Opt2 and DNA-Opt4X) are due to the different ELF algorithms and the different implementations of the low-energy Mott–Coulomb corrections. These differences yield ionization cross sections which differ by up to ~50% at sub-100 eV energies but less than ~10% above ~100 eV. On the other hand, the ionization cross sections of DNA-Opt6, which are calculated by the Binary-Encounter-Bethe (BEB) model [45], are consistently higher, especially for sub-100 eV energies. This is mainly due to the neglect of long-range screening effects in the BEB (being essentially an atomic model). In contrast, differences in the excitation cross section persist over the entire energy range. Specifically, the excitation cross section of the present model (DNA-Opt4X) is consistently larger (by a factor of ~2) from DNA-Opt2 due to differences in the ELF parameterization [43,44]. These differences are further enhanced at very low energies (<50 eV) due to the partitioning algorithm implemented in DNA-Opt4X which re-distributes the oscillator strength below the binding energies of each ionization shell under the constraints of the sum-rules. Interestingly, noticeable higher excitation cross sections are observed for DNA-Opt6 which is based on the dielectric function parameterization of Dingfelder and co-workers [49,54]. Note that DNA-Opt6 uses a hybrid inelastic model with an atomic model for ionizations and a dielectric model of excitations [45].

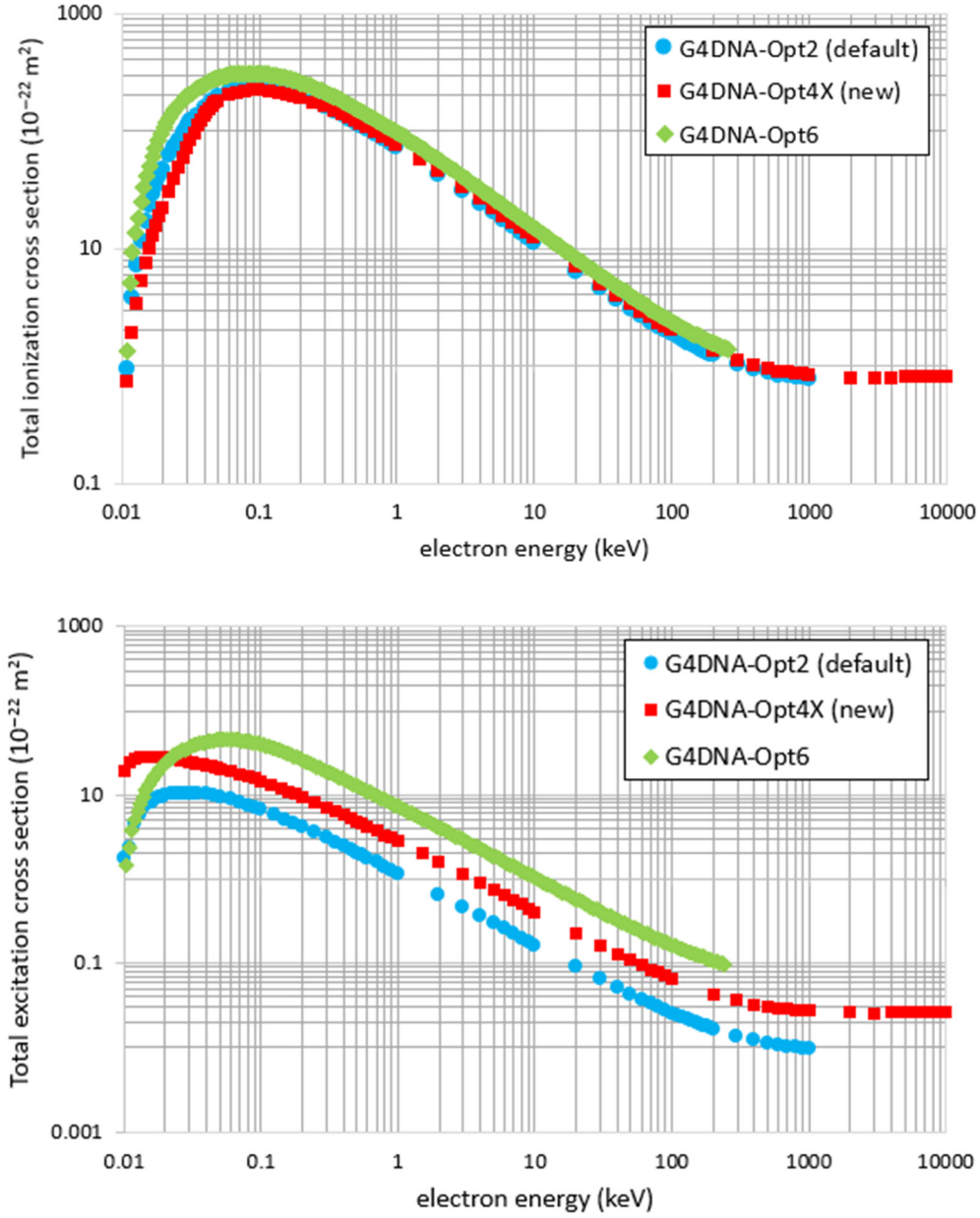

Figure 5. Comparison of the total ionization cross section (**top** panel) and the total excitation cross section (**bottom** panel) of liquid water as a function of electron energy calculated by different Geant4-DNA constructors, namely, DNA-Opt2 (default), DNA-Opt4X (present/new), and DNA-Opt6. Note that each constructor has a different upper energy limit of application (see text).

3.2. Stopping Power Simulations

Figure 6 (top panel) compares the electronic stopping power (hereafter SP) calculated by DNA-Opt2, which extends up to 1 MeV, the present model (DNA-Opt4X), which extends up to 10 MeV, and DNA-Opt6 which extends up to 256 keV. SP values from ICRU Report 90 (which is the most recent ICRU Report on the subject) are also depicted [59]. The simulated SP data have been obtained by the Geant4 example called *spower* [17], which transports the particle in frozen velocity mode. Importantly, in the present context, the SP results depend solely upon the ionization and excitation cross sections implemented into the code (i.e., they are not influenced by the elastic model contained in the corresponding constructors). The statistical uncertainty of the SP data presented is less than 1%. It should be noted that the simulated SP data by the different Geant4-DNA constructors (DNA-Opt2, DNA-Opt4X, DNA-Opt6) are essentially equivalent to the numerical calculation of SP

through Equation (14) using the ionization DCS and excitation TCS of the corresponding constructor. In the bottom panel of Figure 6, the percentage difference in the simulated SP data of each constructor (i.e., inelastic model), from the ICRU values is presented, i.e., $100 \times \frac{SP_{model} - SP_{ICRU}}{SP_{ICRU}}$. The comparison is limited to the ICRU energy range from 1 keV to 10 MeV. Traditionally, ICRU does not provide SP values for electrons at sub-keV energies due to the limitations of the Bethe formula upon which they are based. Specifically, the Bethe SP formula neglects inner-shell corrections and effects beyond the first Born approximation (apart from a kinematic upper cutoff energy limit to knock-on electrons due to indistinguishability). These effects become gradually significant below a few keV. Therefore, the uncertainty of ICRU's SP values is rapidly increasing below 10 keV. In our calculation scheme, inner-shell corrections are automatically included via the dispersion relations that extend ELF to non-zero q, while non-Born effects are included ad hoc through the Mott–Coulomb terms (in addition to the kinematic limit due to indistinguishability).

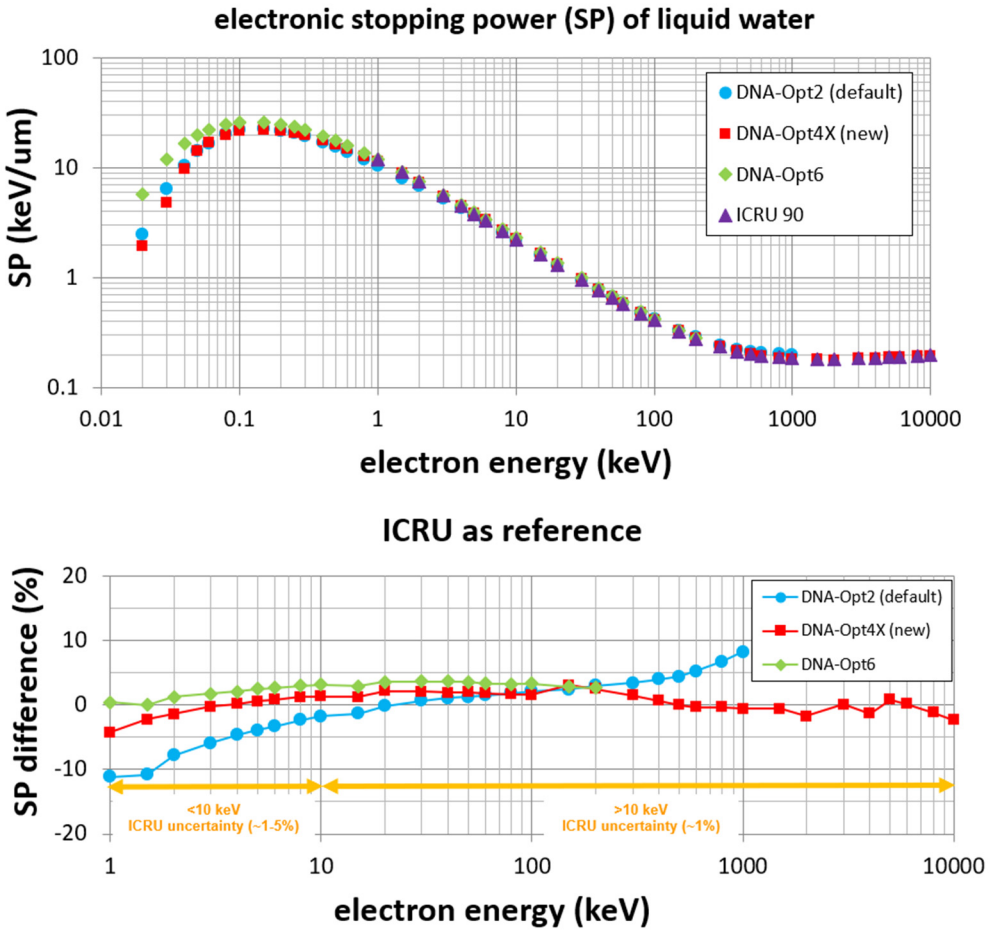

Figure 6. (**Top** panel) Electronic stopping power (SP) of liquid water for electrons over the energy range from 20 eV to 10 MeV simulated by different Geant4-DNA constructors, namely, DNA-Opt2 (default), DNA-Opt4X (present/new), and DNA-Opt6, and compared against the SP values of ICRU Report 90 [59]. (**Bottom** panel) Percentage difference in the various Geant4-DNA constructors from ICRU [59].

It can be seen that the present model (DNA-Opt4X), not only extends the application of Geant4-DNA to higher energies, namely up to 10 MeV (compared to the 1 MeV upper limit of DNA-Opt2 and 256 keV of DNA-Opt6), but also offers much better agreement with the SP values of ICRU Report 90 [59]. Specifically, in the energy range from 10 keV to 10 MeV, where the ICRU values are most reliable (with reported uncertainty at the ~1% level), the present model (DNA-Opt4X) deviates by up to ~3%. In the low energy range of 1–10 keV,

the deviation of DNA-Opt4X from ICRU is between 1 and 5%, which roughly coincides with the reported uncertainty range of the ICRU values [59]. It is noteworthy that the deviation of DNA-Opt2 from ICRU is consistently higher than the present model, reaching up to 10% at both the low and high energy end. Similarly, the deviations of DNA-Opt6 from ICRU are also slightly higher than the present model. In Figure 7, we illustrate the influence of the various corrections implemented into the present model (DNA-Opt4X) (see Figure 1) in the calculation of the SP. Specifically, the percentage difference between the present SP data, calculated with and without the individual corrections, and the ICRU values (which are used for benchmarking), is presented over the energy regime where these corrections are applied, i.e., in accordance with Figure 1, we have split the comparison into the energy regions 1–100 keV (Regime II), 100 keV–1 MeV (Regime III), and 1–10 MeV (Regime IV). Note that the comparison is limited to the energy range from 1 keV to 10 MeV where SP data are provided by ICRU. Evidently, the deviations of the present model from ICRU decrease from ~10–15% (without corrections) to ~3% (with corrections).

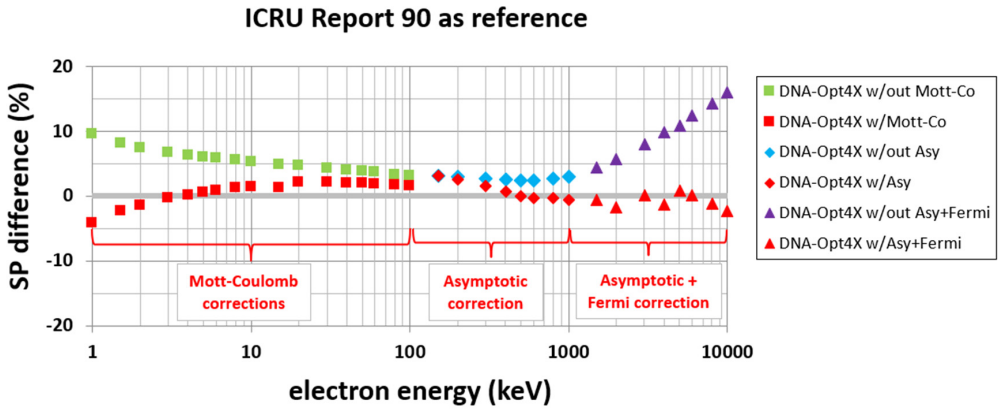

Figure 7. Percentage difference in the electronic stopping power (SP) calculated by the present model (DNA-Opt4X) with and without the various correction terms from the values of ICRU Report 90 [59]. The notation is as follows: "Mott-Co" denotes the Mott–Coulomb low-energy correction (see Section 2.3), "Asy" refers to the high-energy asymptotic correction (see Section 2.4), "Fermi" refers to the (relativistic) Fermi density correction (see Section 2.4).

In Figure 8, we focus on the influence of the low-energy corrections (i.e., the Mott and the Coulomb corrections) on the SP over the energy range where these corrections are applied, i.e., from 10 eV to 100 keV (see Figure 1). Specifically, we depict the ratio of the SP with the corrections to the SP without the corrections, i.e., $\frac{SP_{\text{with corrections}}}{SP_{\text{w/out corrections}}}$. Both the individual and combined effects of the Mott and Coulomb corrections are shown. As expected, the ratio is less than unity at all energies depicted. Specifically, it can be seen that the combined effect of the Mott and Coulomb corrections reduces the SP by up to ~40% at 100 eV and gradually vanishes at 100 keV where the ratio approaches unity ($\geq$0.99), i.e., the effect on SP falls below the 1% level. Therefore, low-energy corrections are included in DNA-Opt4X only in the energy Regimes I and II (see Figure 1).

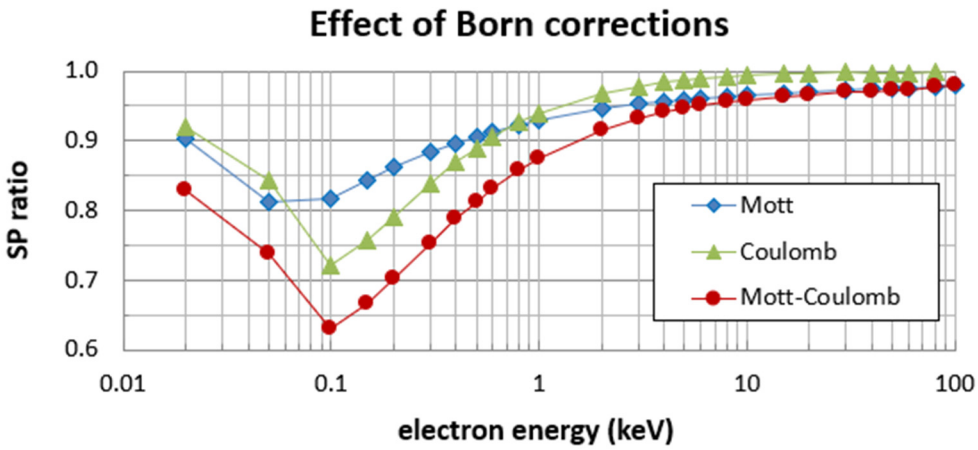

Figure 8. The ratio of the electronic stopping power (SP) with the low-energy corrections (i.e., the Mott and/or the Coulomb corrections) to the SP without the corrections is calculated by the present model (DNA-Opt4X).

3.3. Range Simulations

Another magnitude which depends solely upon the inelastic model (i.e., on the ionization and excitation cross sections) is the pathlength (see Equation (15)). Geant4 offers a ready-to-use example called *range* [17], which calculates (among other things) the average pathlength (or range) of the particle in a medium until its energy falls below a pre-determined cutoff value set by the user (called "tracking cut" in Geant4). Figure 9 presents simulation data of the electron range as a function of the (initial) electron energy with tracking cut set at 10 eV (i.e., T_{final} = 10 eV in Equation (15)) for DNA-Opt2, which extends up to 1 MeV [15,17], the present model (DNA-Opt4X), which extends up to 10 MeV, and DNA-Opt6, which extends up to 256 keV [17,45]. The statistical uncertainty of the data depicted is less than 1%. Range values from ICRU Report 90 are also depicted for comparison [59]. The ICRU values are determined based on the continuous slowing down approximation (CSDA) whereby the range is defined as an integral over the reciprocal SP (see Equation (15)). In the bottom panel of Figure 9, the percentage difference in the simulated range data of each constructor from the ICRU values is presented, i.e., $100 \times \left(\frac{R_{model} - R_{ICRU}}{R_{ICRU}}\right)$. The comparison is limited to electron energies from 1 keV to 10 MeV where ICRU values are available. Note that the uncertainty of the range values given by ICRU increases rapidly below 10 keV. This is due to the limited accuracy of the Bethe SP formula (entering Equation (15)) for energies 1–10 keV (already discussed above) and, most importantly, to the crude (linear) extrapolation of SP from 1 keV down to 0 eV adopted by ICRU in the CSDA calculation via Equation (15). Thus, ICRU's range value below 10 keV should be considered only as qualitative.

The results in Figure 9 indicate that, for energies from 10 keV to 10 MeV, where the ICRU values can be considered most accurate (assuming a similar uncertainty to the ICRU SP data, i.e., ~1%), the present model (DNA-Opt4X) deviates from ICRU by less than 5% and, for energies up to 1 MeV by less than 2%. In contrast, the deviation of DNA-Opt2 from ICRU data is consistently higher (up to 10%) than the present model. The deviations of DNA-Opt6 from ICRU are within 1%. Thus, the present model (DNA-Opt4X) not only extends the application of Geant4-DNA to higher energies (up to 10 MeV) compared to DNA-Opt2 (upper limit 1 MeV) and DNA-Opt6 (upper limit 256 keV) but also offers much better agreement with the range data of the ICRU Report 90, as also observed for the SP data (Figure 6 of Section 3.2).

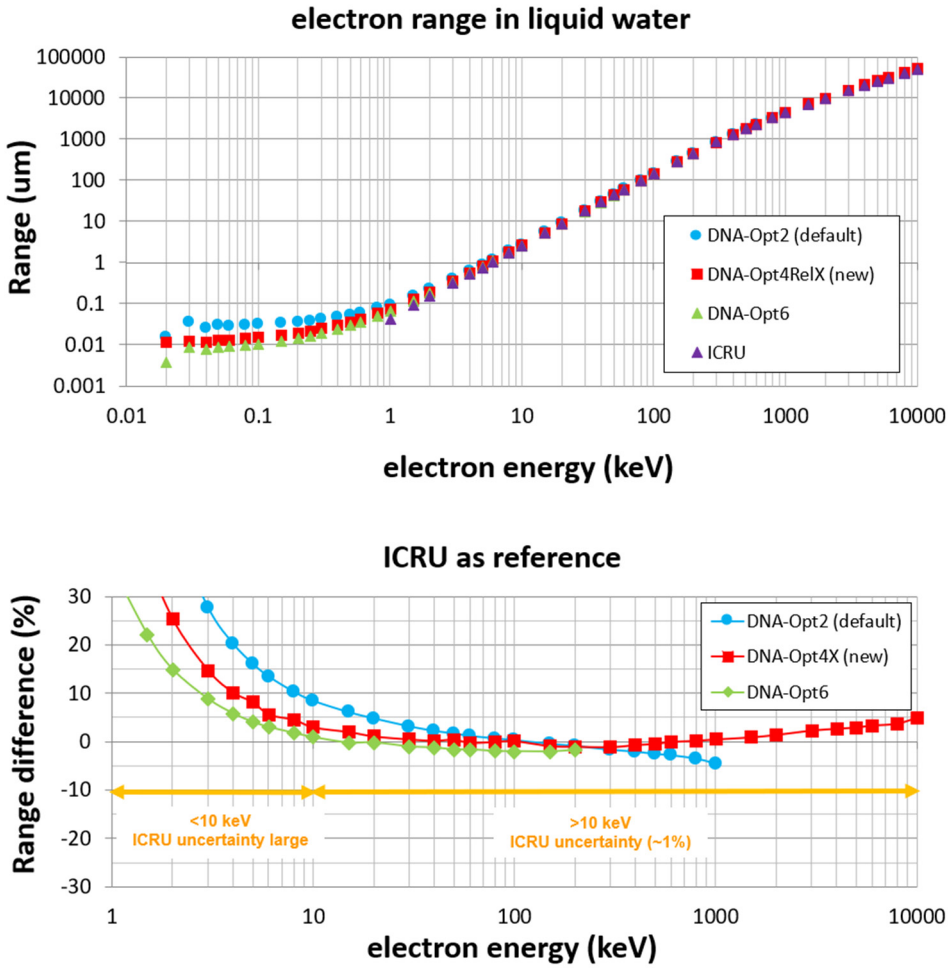

Figure 9. (**Top** panel) range (or average pathlength) of electrons in liquid water over the energy range from 20 eV up to 10 MeV simulated by different Geant4-DNA constructors, namely, DNA-Opt2 (default), DNA-Opt4X (present/new), and DNA-Opt6, and compared against the range values of ICRU Report 90 [59]; (**Bottom** panel) Percentage difference in the various Geant4-DNA constructors from ICRU [59].

4. Conclusions

The recommended Geant4-DNA inelastic constructor (DNA-Opt4) for low-energy track-structure simulations has been improved and extended from 10 keV to 10 MeV using the relativistic plane wave Born approximation and other theoretical considerations. Based on this development, a full set of differential and total ionization and electronic excitation cross sections, spanning the energy range from 10 eV to 10 MeV, has been calculated and implemented into Geant4-DNA via a new constructor called DNA-Opt4X. Benchmark simulations of the electronic stopping power and range (or average pathlength) by DNA-Opt4X are carried out and shown to be in almost excellent agreement (at the few % level) with the latest ICRU recommendations. The present results offer significant improvement (by a factor of ~2) over the default Geant4-DNA constructor (DNA-Opt2) and an order-of-magnitude higher electron transport limit. This development will allow Geant4-DNA users to perform for the first time electron track-structure simulations, including nano- and micro-dosimetry calculations, up to 10 MeV, thus, covering a wider range of radiotherapeutic applications, including FLASH EBRT, as well as space applications involving MeV electron which are not currently reachable by the existing Geant4-DNA constructors.

Author Contributions: Conceptualization, D.E., I.K., S.I. and V.I.; methodology, I.K. and D.E.; software, I.K., S.I. and H.N.T.; validation, I.K. and H.N.T.; formal analysis, I.K. and D.E.; investigation,

I.K. and D.E.; data curation, I.K. and D.E.; writing—original draft preparation, I.K.; writing—review and editing, D.E., I.K., S.I., V.I., S.G., L.D. and H.N.T.; supervision, D.E., I.K. and S.I.; project administration, I.K., D.E., S.I., G.S. and P.N.; funding acquisition, D.E., I.K., S.I., L.D., G.S. and P.N. All authors have read and agreed to the published version of the manuscript.

Funding: This research was funded by the European Space Agency (ESA) under contract "BioRad III" No. 4000132935/21/NL/CRS (2021–2023) as well as the project FNS Synergia grant MAGIC-FNS CRS II5_186369.

Institutional Review Board Statement: Not applicable.

Informed Consent Statement: Not applicable.

Data Availability Statement: The original contributions presented in the study are included in the article, further inquiries can be directed to the corresponding author.

Conflicts of Interest: The authors declare no conflicts of interest.

List of Abbreviations

BEAX	Binary Encounter Approximation with Exchange
DCS	Differential Cross Section
EBRT	Electron Beam Radiation Therapy
ELF	Energy Loss Function
ICRU	International Commission on Radiation Units and Measurements
Geant	Geometry And Tracking
MCTS	Monte Carlo Trak Structure
PWBA	Plane Wave Born Approximation
RPWBA	Relativistic Plane Wave Born Approximation
RT	Radiation Therapy
SP	Stopping Power
TCS	Total Cross Section
CSDA	Continuous Slowing Down Approximation

List of Nomenclature

symbol	**nomenclature**	**dimensional units**
T	kinetic energy	energy
E	energy transfer	energy
q	momentum transfer	(mass)·(length)·(time)$^{-1}$
ε	dielectric function	–
σ	cross section	(length)^2
α_0	Bohr radius	length
N	density of water molecules	(length)$^{-3}$
B	binding energy	energy
U	average kinetic energy in shell	energy
m	electron rest mass	mass
β	particle velocity over speed of light	–
c	speed of light	(length)·(time)$^{-1}$
Q	recoil energy	energy
R	range	length

References

1. Nikjoo, H.; Emfietzoglou, D.; Liamsuwan, T.; Taleei, R.; Liljequist, D.; Uehara, S. Radiation track, DNA damage and response-a review. *Rep. Prog. Phys.* **2016**, *79*, 116601. [CrossRef]
2. Nikjoo, H.; O'Neill, P.; Terrissol, M.; Goodhead, D.T. Modelling of radiation induced DNA damage: The early physical and chemical event. *Int. J. Radiat. Biol.* **1994**, *66*, 453–457. [CrossRef] [PubMed]
3. Muroya, Y.; Meesugnoen, J.; Jay-Gerin, J.P.; Filali-Mouhim, A.; Goulet, T.; Katsumura, Y.; Mankhetkorn, S. Radiolysis of liquid water: An attempt to reconcile Monte-Carlo simulations with new experimental hydrated electron yield data at early times. *Can. J. Chem.* **2002**, *80*, 1367–1374. [CrossRef]
4. Plante, I. A review of simulation codes and approaches for radiation chemistry. *Phys. Med. Biol.* **2021**, *66*, 03TR02. [CrossRef]
5. Tran, H.N.; Archer, J.; Baldacchino, G.; Brown, J.M.; Chappuis, F.; Cirrone, G.A.P.; Desorgher, L.; Dominguez, N.; Fattori, S.; Guatelli, S.; et al. Review of chemical models and applications in Geant4-DNA: Report from the ESA BioRad III Project. *Med. Phys.* **2024**, *51*, 5873–5889. [CrossRef] [PubMed]
6. Nikjoo, H.; Uehara, S.; Emfietzoglou, D.; VCucinotta, F.A. Track structure codes in radiation research. *Radiat. Meas.* **2006**, *41*, 1052–1074. [CrossRef]
7. Chatzipapas, K.P.; Papadimitroulas, P.; Emfietzoglou, D.; Kalospyros, S.A.; Hada, M.; Georgakilas, A.G.; Kagadis, G.C. Ionizing Radiation and Complex DNA Damage: Quantifying the Radiobiological Damage Using Monte Carlo Simulations. *Cancers* **2020**, *12*, 799. [CrossRef] [PubMed]
8. Kyriakou, I.; Sakata, D.; Tran, H.N.; Perrot, Y.; Shin, W.G.; Lampe, N.; Zein, S.; Bordage, M.C.; Guatelli, S.; Villagrasa, C.; et al. Review of the Geant4-DNA simulation toolkit for radiobiological applications at the cellular and DNA level. *Cancers* **2022**, *14*, 35. [CrossRef]
9. Emfietzoglou, D.; Nikjoo, H. The effect of model approximations on single-collision distributions of low-energy electrons in liquid water. *Radiat. Res.* **2005**, *163*, 98–111. [CrossRef] [PubMed]
10. Dingfelder, M.; Ritchie, R.H.; Turner, J.E.; Friedland, W.; Paretzke, H.G.; Hamm, R.N. Comparisons of Calculations with PARTRAC and NOREC: Transport of Electrons in Liquid Water. *Radiat. Res.* **2008**, *169*, 584–594. [CrossRef] [PubMed]
11. Emfietzoglou, D.; Kyriakou, I.; Abril, I.; Garcia-Molina, R.; Nikjoo, H. Inelastic scattering of low-energy electrons in liquid water computed from optical-data models of the Bethe surface. *Int. J. Radiat. Biol.* **2011**, *88*, 22–28. [CrossRef]
12. Emfietzoglou, D.; Papamichael, G.; Nikjoo, H. Monte Carlo electron track structure calculations in liquid water using a new model dielectric response function. *Radiat. Res.* **2017**, *188*, 355–368. [CrossRef] [PubMed]
13. Pater, P.; Seuntjens, J.; Naqa, I.E.; Bernal, M.A. On the consistency of Monte Carlo track structure DNA damage simulations. *Med. Phys.* **2014**, *41*, 121708. [CrossRef] [PubMed]
14. Incerti, S.; Baldacchino, G.; Bernal, M.; Capra, R.; Champion, C.; Francis, Z.; Guèye, P.; Mantero, A.; Mascialino, B.; Moretto, P.; et al. The Geant4-DNA project. *Int. J. Model. Simul. Sci. Comput.* **2010**, *1*, 157–178. [CrossRef]
15. Incerti, S.; Ivanchenko, A.; Karamitros, M.; Mantero, A.; Moretto, P.; Tran, H.N.; Mascialino, B.; Champion, C.; Ivanchenko, V.N.; Bernal, M.A.; et al. Comparison of GEANT4 very low energy cross section models with experimental data in water. *Med. Phys.* **2010**, *37*, 4692–4708. [CrossRef] [PubMed]
16. Bernal, M.A.; Bordage, M.C.; Brown, J.M.C.; Davídková, M.; Delage, E.; El Bitar, Z.; Enger, S.A.; Francis, Z.; Guatelli, S.; Ivanchenko, V.N.; et al. Track structure modeling in liquid water: A review of the Geant4-DNA very low energy extension of the Geant4 Monte Carlo simulation toolkit. *Phys. Med.* **2015**, *31*, 861–874. [CrossRef]
17. Incerti, S.; Kyriakou, I.; Bernal, M.A.; Bordage, M.C.; Francis, Z.; Guatelli, S.; Ivanchenko, V.; Karamitros, M.; Lampe, N.; Lee, S.B.; et al. Geant4-DNA example applications for track-structure simulations in liquid water. A report from the Geant4-DNA project. *Med. Phys.* **2018**, *45*, 722–739. [CrossRef] [PubMed]
18. Kyriakou, I.; Ivanchenko, V.; Sakata, D.; Bordage, M.C.; Guatelli, S.; Incerti, S.; Emfietzoglou, D. Influence of track structure and condensed history physics models of Geant4 to nanoscale electron transport in liquid water. *Phys. Med.* **2019**, *58*, 149–154. [CrossRef]
19. Favaudon, V.; Caplier, L.; Monceau, V.; Pouzoulet, F.; Sayarath, M.; Fouillade, C.; Poupon, M.F.; Brito, I.; Hupé, P.; Bourhis, J.; et al. Ultrahigh dose-rate FLASH irradiation increases the differential response between normal and tumor tissue in mice. *Sci. Transl. Med.* **2014**, *6*, 245ra93. [CrossRef]
20. Schuler, E.; Trovati, S.; King, G.; Lartey, F.; Rafat, M.; Villegas, M.; Praxel, A.J.; Loo, B.W., Jr.; Maxim, P.G. Experimental platform for ultra-high dose rate FLASH irradiation of small animals using a clinical linear accelerator. *Radiat. Oncol. Biol. Phys.* **2017**, *97*, 195–203. [CrossRef] [PubMed]
21. Vozenin, M.C.; De Fornel, P.; Petersson, K.; Favaudon, V.; Jaccard, M.; Germond, J.F.; Petit, B.; Burki, M.; Ferrand, G.; Patin, D.; et al. The advantage of FLASH radiotherapy confirmed in mini-pig and cat-cancer patients. *Clin. Cancer Res.* **2019**, *25*, 35–42. [CrossRef]
22. Wilson, J.D.; Hammond, E.M.; Higgins, G.S.; Petersson, K. Ultra-High Dose Rate (FLASH) radiotherapy: Silver Bullet or Fool's Gold? *Front. Oncol.* **2020**, *9*, 1563. [CrossRef]

23. Nikjoo, H.; Emfietzoglou, D.; Watanabe, R.; Uehara, S. Can Monte Carlo track structure codes reval reaction mechanism in DNA damage and improve radiation therapy? *Radiat. Phys. Chem.* **2008**, *77*, 1270–1279. [CrossRef]
24. El Naqa, I.; Pater, P.; Seuntjens, J. Monte Carlo role in radiobiological modelling of radiotherapy outcomes. *Phys. Med. Biol.* **2012**, *57*, R75. [CrossRef]
25. Brahme, A. Optimized radiation therapy based on radiobiological objectives. *Semin. Radiat. Oncol.* **1999**, *9*, 35–47. [CrossRef]
26. Friendland, W.; Aschmidtt, E.; Kundrat, P.; Dingfelder, M.; Baiocco, G.; Barbieri, S.; Ottolenghi, A. Comprehensive track-structure based evaluation of DNA damage by light ions from radiotherapy-relevant energies down to stopping. *Sci. Rep.* **2017**, *7*, 45161.
27. Huq, M.S.; Sing, H.; Andreo, P.; Houser, C.J. Reference dosimetry in clinical high-energy beams: Comparison of the AAPM TG-51 and AAPM TG-21 dosimetry protocols. *Med. Phys.* **2001**, *28*, 2077–2087. [CrossRef]
28. Durante, M.; Cucinotta, F. Physical basis of radiation protection in space travel. *Rev. Mod. Phys.* **2011**, *83*, 1245–1281. [CrossRef]
29. McKenna-Lawlor, S.; Concalves, P.; Keating, A.; Reitz, G.; Matthia, D. Overview of energetic partic;e hazards during prospective manned missions to Mars. *Planet. Space Sci.* **2012**, *63–64*, 123–132. [CrossRef]
30. Straume, T.; Slaba, T.C.; Bhattacharya, S.; Braby, L.A. Cosmic -ray interaction data for designing biological experiments in space. *Life Sci. Space Res.* **2017**, *13*, 51–59. [CrossRef]
31. Walsh, L.; Schneider, U.; Fogtman, A.; Kausch, C.; McKenna-Lawlor, S.; Narici, L.; Ngo-Anh, J.; Reitz, G.; Sabatier, L.; Santin, G.; et al. Research plans in Europe for radiation health hazard assessment in exploratory space missions. *Life Sci. Space Res.* **2019**, *21*, 73–82. [CrossRef] [PubMed]
32. Strigari, L.; Strolin, S.; Morganti, A.G.; Bartoloni, A. Dose-effects models for space radiobiology: An overview on dose-effects relationships. *Front. Public Health* **2021**, *9*, 733337. [CrossRef] [PubMed]
33. Cuccinotta, F.A. Flying without a net: Space radiation cancer risk predictions without a gamma-ray basis. *Int. J. Mol. Sci.* **2022**, *23*, 4324. [CrossRef]
34. Chancellor, J.; Nowadly, C.; Williams, J.; Aunon-Chancellor, S.; Chesal, M.; Looper, J.; Newhauser, W. Everything you wanted to know about space radiation but were afraid to ask. *J. Environ. Sci. Health Part C* **2021**, *39*, 113–128. [CrossRef] [PubMed]
35. Shuryak, I.; Slaba, T.C.; Plante, I.; Poignant, F.; Blattnig, S.R.; Brenner, D.J. A practical approach for conituous in situ characterization of radiation quality factors in space. *Sci. Rep.* **2022**, *12*, 1453. [CrossRef]
36. Papadopoulos, A.; Kyriakou, I.; Incerti, S.; Santin, G.; Nieminen, P.; Daglis, I.A.; Li, W.; Emfietzoglou, D. Space radiation qualiy factor for Galactic Cosmic Rays and typical space mission scenarios using a microdosimetric approach. *Radiat. Environ. Biophys.* **2023**, *62*, 221–234. [CrossRef] [PubMed]
37. Chappuis, F.; Tran, H.N.; Zein, S.A.; Bailat, C.; Incerti, S.; Bochud, F.; Desorgher, L. The general-purpose Geant4 Monte Carlo toolkit and its Geant4-DNA extension to investigate mechanisms underlying the FLASH effect in radiotherapy: Current status and challenges. *Phys. Med.* **2023**, *110*, 102601. [CrossRef] [PubMed]
38. Spitz, D.R.; Buettner, G.R.; Petronek, M.S.; St-Aubin, J.J.; Flynn, R.T.; Waldron, T.J.; Limoli, C.L. An integrated physico-chemical approach for explaining the differential impact of FLASH versus conventional dose rate irradiation on cancer and normal tissue responses. *Radiother. Oncol.* **2019**, *139*, 23–27. [CrossRef]
39. Alanazi, A.; Meesungnoen, J.; Jay-Gerin, J.-P. A Computer Modeling Study of Water Radiolysis at High Dose Rates. Relevance to FLASH Radiotherapy. *Radiat. Res.* **2021**, *95*, 149–162. [CrossRef] [PubMed]
40. Bug, M.U.; Baek, W.Y.; Rabus, H.; Villagrasa, C.; Meylan, S.; Rosenfeld, A. An electron-impact cross section data set (10 eV–1 keV) of DNA constituents based on consistent experimental data: A requisite for Monte Carlo simulations. *Radiat. Phys. Chem.* **2017**, *130*, 459–479. [CrossRef]
41. Zein, S.A.; Bordage, M.-C.; Francis, Z.; Macetti, G.; Genoni, A.; Cappello, C.D.; Shin, W.-G.; Incerti, S. Electron transport in DNA bases: An extension of the Geant4-DNA Monte Carlo toolkit. *Nucl. Instrum. Methods Phys. Res. B Beam Interact. Mater. At.* **2021**, *488*, 70–82. [CrossRef]
42. Kyriakou, I.; Incerti, S.; Francis, Z. Technical note: Improvements in Geant4 energy-loss model and the effect on low-energy electron transport in liquid water. *Med. Phys.* **2015**, *42*, 3870–3876. [CrossRef]
43. Kyriakou, I.; Šefl, M.; Nourry, V.; Incerti, S. The impact of new geant4-DNA cross section models on electron track structure simulations in liquid water. *J. Appl. Phys.* **2016**, *119*, 194902. [CrossRef]
44. Bordage, M.C.; Bordes, J.; Edel, S.; Terrissol, M.; Franceries, X.; Bardiès, M.; Lampe, N.; Incerti, S. Implementation of new physics models for low energy electrons in liquid water in Geant4-DNA. *Phys. Med.* **2016**, *32*, 1833–1840. [CrossRef] [PubMed]
45. Nikjoo, H.; Uehara, S.; Emfietzoglou, D. *Interaction of Radiation with Matter*; CRC Press Taylor & Francis: Boca Raton, FL, USA, 2012.
46. Powell, C.J.; Jablonski, A. Evaluation of calculated and measured electron inelastic mean free paths near solid surfaces. *J. Phys. Chem. Ref. Data* **1999**, *28*, 19–62. [CrossRef]
47. De Vera, P.; Garcia-Molina, R. Electron inelastic mean free paths in condensed matter down to a few electronvolts. *J. Phys. Chem. C* **2019**, *123*, 2075–2083. [CrossRef]

48. Dingfelder, M. Updated model for dielectric response function of liquid water. *Appl. Radiat. Isot.* **2014**, *83*, 142–147. [CrossRef] [PubMed]
49. Kyriakou, I.; Emfietzoglou, D.; Incerti, S. Status and Extension of the Geant4-DNA Dielectric Models for Application to Electron Transport. *Front. Phys.* **2022**, *9*, 711317. [CrossRef]
50. Taioli, S.; Trevisanutto, P.E.; de Vera, P.; Simonucci, S.; Abril, I.; Garcia-Molina, R.; Dapor, M. Relative Role of Phsyical Mechanisms on Complex Biodamage Induced by Carbon Irradiation. *J. Phys. Chem. Lett.* **2021**, *12*, 487–493. [CrossRef]
51. Koval, N.E.; Koval, P.; Da Pieve, F.; Kohanoff, J.; Artacho, E.; Emfietzoglou, D. Inelastic scattering of electrons in water from first-principles: Cross sections and inelaqstic mean free path for use in Monte Carlo track-structure simulations of biological damage. *R. Soc. Open Sci.* **2021**, *9*, 212011. [CrossRef]
52. Semenenko, V.A.; Turner, J.E.; Borak, T.B. NOREC, a Monte Carlo code for simulating electron tracks in liquid water. *Radiat. Environ. Biophys.* **2003**, *42*, 213–217. [CrossRef] [PubMed]
53. Dingfelder, M.; Hantke, D.; Inokuti, M.; Paretzke, H.G. Electron inelastic-scattering cross sections in liquid water. *Radiat. Phys. Chem.* **1998**, *53*, 1–18. [CrossRef]
54. Liamsuwan, T.; Emfietzoglou, D.; Uehara, S.; Nikjoo, H. Microdosimetry of low-energy electrons. *Int. J. Radiat. Biol.* **2012**, *88*, 899–907. [CrossRef]
55. ICRU. *Secondary Electron Spectra from Charged Particle Interactions*; Report 55; International Commission of Radiation Units and Measurements: Bethesda, MD, USA, 1996.
56. Llovet, X.; Powell, C.J.; Salvat, F.; Jablonski, A. Cross Sections for Inner Shell Ionization by Electron Impact. *J. Phys. Chem. Ref. Data* **2014**, *43*, 013102. [CrossRef]
57. Fernández-Varea, J.M.; Llovet, X.; Salvat, F. Cross sections for electron interactions in condensed matter. *Surf. Interface Anal.* **2005**, *27*, 824–832. [CrossRef]
58. ICRU. *Key Data for Ionizing Radiation Dosimetry: Measurement Standards and Applications*; Report 90; International Commission of Radiation Units and Measurements: Bethesda, MD, USA, 2016.
59. Fano, U. Differential inelastic scattering of relativistic charged particles. *Phys. Rev.* **1956**, *102*, 385–387. [CrossRef]
60. Fano, U. Penetration of protons, alpha particles, and mesons. *Annu. Rev. Nucl. Sci.* **1963**, *13*, 1–66. [CrossRef]
61. Steinheimer, R.M.; Berger, M.J.; Seltzer, S.M. Density effect for the ionization loss of charged particles in various substances. *At. Data Nucl. Data Tables* **1984**, *30*, 261–271. [CrossRef]